



Robust long-range magnetic correlation across antiphase domain boundaries in Sr₂CrReO₆Bo Yuan ¹, Subin Kim,¹ Sae Hwan Chun,¹ Wentao Jin,² C. S. Nelson,³ Adam J. Hauser ⁴, F. Y. Yang,⁵ and Young-June Kim¹¹*Department of Physics, University of Toronto, Toronto, Ontario, Canada M5S 1A7*²*School of Physics, Key Laboratory of Micro-Nano Measurement-Manipulation and Physics (Ministry of Education), Beihang University, Beijing 100191, China*³*National Synchrotron Light Source II, Brookhaven National Laboratory, Upton, New York 11973, USA*⁴*Department of Physics and Astronomy, The University of Alabama, Tuscaloosa, Alabama 35487, USA*⁵*Department of Physics, The Ohio State University, Columbus, Ohio 43210, USA*

(Received 24 September 2020; revised 15 January 2021; accepted 25 January 2021; published 5 February 2021)

We report a resonant elastic x-ray scattering study of a thin-film sample of Sr₂CrReO₆, which has one of the highest ferrimagnetic transition temperatures among ordered double perovskites. We found resonantly enhanced magnetic Bragg peaks at $\mathbf{Q} = (\text{odd}, \text{odd}, \text{odd})$ at both the rhenium L_2 and L_3 edges, which coincide with the structural Bragg peaks of Sr₂CrReO₆. By analyzing the widths of these Bragg peaks, we extracted very different structural and magnetic correlation lengths. The former is about 15 nm, while the latter is constrained by the instrumental resolution to be at least 90 nm. We argue that a finite structural correlation length is consistent with the existence of antiphase nanodomains in our sample. On the other hand, a much larger magnetic correlation length indicates that the magnetic correlation extends far beyond the boundaries of individual domains and is consistent with strong antiferromagnetic coupling between different antiphase domains. Last, from the azimuthal dependence of the magnetic intensity, we show that the magnetic moments lie perpendicular to the c axis, which explains the earlier bulk magnetization data.

DOI: [10.1103/PhysRevB.103.064410](https://doi.org/10.1103/PhysRevB.103.064410)**I. INTRODUCTION**

Ordered double perovskite (DP), $A_2BB'O_6$, has been intensively studied as one of the most promising candidates for spintronic materials. In an ideal DP, the transition metal B and B' ions are alternately arranged in a rocksalt structure, surrounded by corner-sharing oxygen octahedra [see Fig. 1(a)]. A strong hybridization between B and B' ions can potentially lead to a very high magnetic ordering temperature T_C and a large spin polarization at the Fermi level. These properties give rise to a large magnetoresistance at room temperature essential for spintronic applications [1]. The most well known example is Sr₂FeMoO₆ with $T_C \sim 420$ K [2,3]. It was later surpassed by Sr₂CrReO₆ [4–8] and Sr₂CrOsO₆ [9–11] with even higher T_C 's of 635 and 725 K, respectively. However, one important issue that inevitably arises during the synthesis of a DP sample is antisite (AS) disorder, whereby locations of B and B' are exchanged in finite regions of the sample. One might naïvely expect that the AS disorder occurs as a random point defect when a site is occupied by a *wrong* atom (B' in the B site, for example). While this random occupancy model is useful in distinguishing an ordered DP sample from its fully disordered limit (a solid solution of B and B' in a regular perovskite structure), it is an inaccurate picture for describing the AS disorder in most ordered DP samples. In a more realistic description, AS disorder actually exists as a planar defect known as an antiphase boundary (APB), which separates two adjacent antiphase domains (APDs) whose B/B' arrangement is reversed. Note that there is no *wrong* atom in this picture: Each APD is perfectly ordered, and the only

defects are the APBs consisting of B - O - B or B' - O - B' bonds. This picture is supported by Mössbauer spectroscopy [12] as well as transmission electron microscopy (TEM) studies [13–15]. A recent quantitative scanning TEM study directly imaged the APB in a high-quality Sr₂CrReO₆ film [16]. In addition, an x-ray absorption fine-structure study [17] also revealed that small APDs persist even in highly disordered DP samples of Sr₂FeMoO₆.

An important question is the effect AS disorder on a DP sample's magnetic properties, which directly affect its functionality as a spintronic material. Previous bulk magnetization [18,19] and x-ray magnetic circular dichroism (XMCD) [20] studies revealed that the magnetization is reduced with an increasing level of AS disorder. However, these techniques measure only the total magnetic response, which is averaged over all APDs. Thus, these studies have not addressed the most important aspect of the question, namely, how the neighboring APDs are correlated magnetically. Since magnetically correlated APDs are much easier to manipulate than random ones, one expects a larger magnetoresistance in the former and hence better performance as a spintronic material [13,21]. The relationship between the APB and magnetic domains has been the topic of a number of studies. In a TEM study of a Ba₂FeMoO₆ single-crystal sample, Asaka *et al.* found large APDs of a few hundred nanometers and a strong pinning of magnetic domain boundaries at the APB [15]. However, *quantitative* information regarding how magnetic order propagates across APBs on a microscopic level is still lacking.

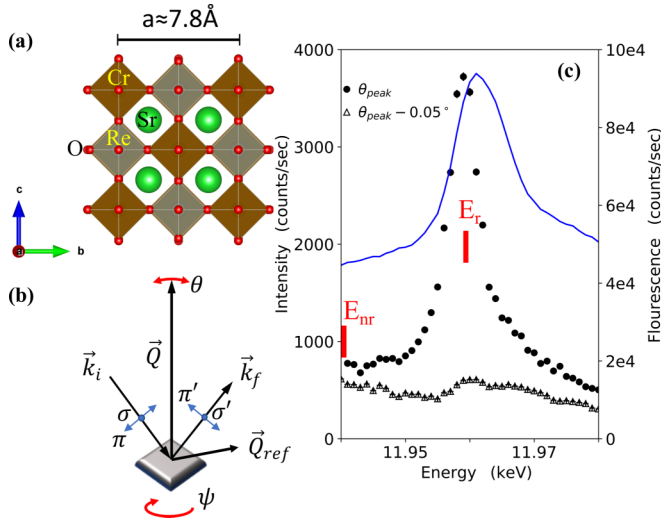


FIG. 1. (a) Unit cell of an ideal double perovskite. Throughout the paper, we use cubic notation with $a \approx 7.8 \text{ \AA}$. (b) Experimental setup for resonant elastic x-ray scattering. The angle θ denotes a rotation within the scattering plane, and the azimuthal angle ψ denotes a rotation of the sample around the momentum transfer $\mathbf{Q} = \mathbf{k}_f - \mathbf{k}_i$. $\psi = 0$ is defined as the sample orientation where the reference wave vector $\mathbf{Q}_{\text{ref}} = (1, 1, 0)$ is in the scattering plane, as shown. An x-ray can be polarized either parallel or perpendicular to the scattering plane, denoted by σ and π polarizations, respectively. Polarizations of outgoing x rays are denoted with a prime. (c) Energy dependence of the σ - π' channel elastic intensity at $\mathbf{Q} = (1, 1, 5)$ at the Re L_2 edge. The energy dependence is obtained for different θ 's. The solid black circles are the energy dependence at the peak θ value, or θ_{peak} , while open triangles are for the background scan obtained 0.05° away from θ_{peak} . The energy dependence of x-ray fluorescence is shown by the blue solid line.

In this paper, we address this important question using resonant elastic x-ray scattering (REXS), which is a bulk-sensitive technique like neutron scattering. However, since its momentum resolution is much better than that of neutron scattering, it is an ideal probe for extracting quantitative information such as the correlation length. We have applied this technique to understand the room-temperature magnetic and structural correlations in a thin-film sample of $\text{Sr}_2\text{CrReO}_6$ grown on SrTiO_3 with a thickness of 319 nm. At both the Re L_2 and L_3 edges, resonantly enhanced magnetic Bragg peaks are found at $\mathbf{Q} = (\text{odd}, \text{odd}, \text{odd})$, which coincide with the structural Bragg peaks of $\text{Sr}_2\text{CrReO}_6$. Magnetic moments are shown to lie perpendicular to the c axis from the azimuthal dependence of the magnetic intensity. By studying the widths of the structural and magnetic Bragg peaks at $\mathbf{Q} = (\text{odd}, \text{odd}, \text{odd})$, we extracted very different structural and magnetic correlation lengths in the sample. The structural correlation length is $\sim 15 \text{ nm}$, consistent with the existence of APDs of $\sim 15 \text{ nm}$ in our sample. On the other hand, we found the magnetic correlation to be at least 90 nm, far exceeding the average APD size. Our results therefore provide compelling evidence for robust magnetic correlation across the APBs, which we argue to be a consequence of strong antiferromagnetic coupling between neighboring APDs.

II. EXPERIMENTAL DETAILS

In the REXS experiment schematically shown in Fig. 1(b), magnetic scattering is enhanced by tuning the incident photon energy to an atomic absorption edge. The polarization dependence of the scattered x ray distinguishes magnetic scattering from the usual charge scattering, thus allowing both the structural and magnetic information to be obtained. For an incident polarization perpendicular to the scattering plane σ , charge and magnetic scattering give rise to outgoing x-ray polarizations that are perpendicular (σ') and parallel (π') to the scattering plane [22], respectively.

REXS measurements at the rhenium L_2 and L_3 edges were carried out on a 319-nm $\text{Sr}_2\text{CrReO}_6$ thin film grown on SrTiO_3 at beamline 4-ID of the National Synchrotron Light Source (NSLS) II at the Brookhaven National Laboratory. (Details of sample growth were reported in Ref. [5].) Outgoing x-ray polarizations are selected using an aluminum-(4,4,0) and graphite-(0,0,8) analyzer near the L_2 and L_3 edges, respectively. Other than the temperature dependence data shown in Fig. 2(d), all other measurements were carried out at room temperature in air. The temperature of the sample was varied using a hot-air blower and measured using a thermocouple. Sample characterization (see the Supplemental Material [23]) of the 319-nm thin film and a 90-nm $\text{Sr}_2\text{CrReO}_6$ thin film using nonresonant x-ray diffraction was carried out on a Rigaku Smartlab x-ray diffractometer. Magnetization measurement (see the Supplemental Material [23]) was carried out using a Quantum Design superconducting quantum interference device magnetic properties measurement system.

III. EXPERIMENTAL RESULTS

A. L_2 edge

In Fig. 1(c), we show the σ - π' channel resonant intensity at the $\mathbf{Q} = (1, 1, 5)$ Bragg peak as a function of incident photon energy at the Re L_2 edge (black solid circles). The x-ray absorption spectrum as a function of energy (blue solid line) is also shown for comparison. The resonance peak energy at $E_r = 11.959 \text{ keV}$ occurs slightly below the absorption maximum (so-called white line), consistent with REXS studies on other $5d$ rhenium [24,25] and iridium compounds [26–29]. However, the elastic intensity does not disappear when the incident energy is tuned to an energy well below the absorption edge (e.g., $E_{\text{nr}} = 11.94 \text{ keV}$). This indicates that in addition to the resonant diffraction intensity, a nonresonant background is also present at this \mathbf{Q} . In Fig. 1(c), we also show the energy dependence of the intensity slightly off the Bragg peak position, obtained by rotating the sample angle θ [see Fig. 1(b) for definition] by 0.05° away from the exact location of the Bragg peak. A very different energy dependence is obtained at this new position: The resonant feature is clearly absent while the nonresonant background remains. This indicates that the background has a much broader momentum dependence than the main resonant feature.

To further illustrate this, we carried out θ scans at $\mathbf{Q} = (1, 1, 5)$ using the resonant (E_r) and nonresonant (E_{nr}) incident energies. The resultant rocking curves are shown in Fig. 2(a). For the resonant energy E_r (solid circles), the rocking curve consists of a sharp peak on top of a broad

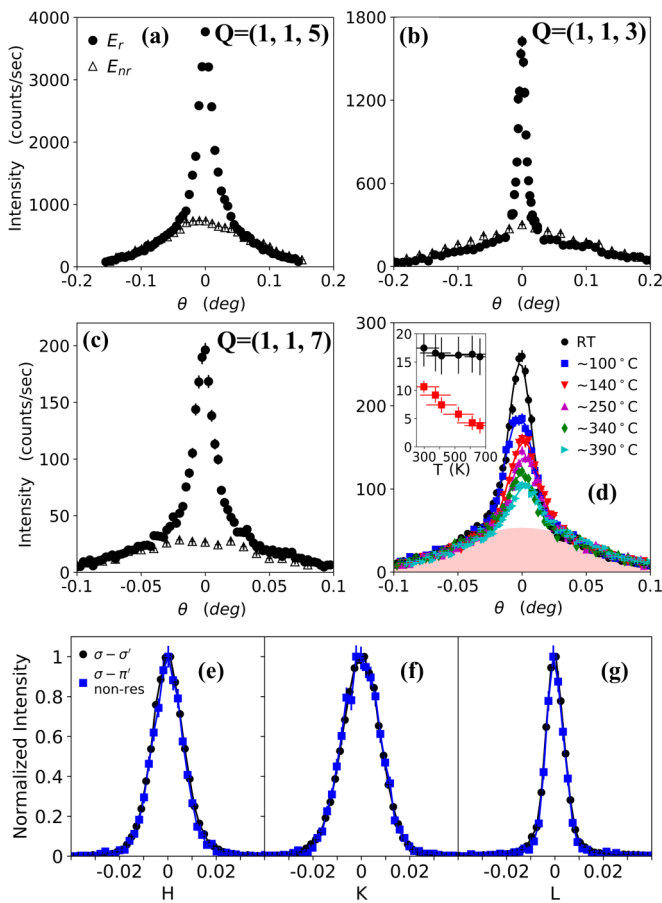


FIG. 2. Rocking curve, or θ scans, at (a) $\mathbf{Q} = (1, 1, 5)$, (b) $\mathbf{Q} = (1, 1, 3)$, and (c) $\mathbf{Q} = (1, 1, 7)$ in the $\sigma\text{-}\pi'$ channel. The two incident energies, $E_r = 11.959$ keV and $E_{nr} = 11.94$ keV, are indicated by vertical lines in Fig. 1(c). (d) Temperature dependence of the rocking curves at $\mathbf{Q} = (1, 1, 7)$ obtained with the resonant incident energy E_r in the $\sigma\text{-}\pi'$ channel. All curves have been shifted horizontally to match the peak positions. The shaded region denotes the nonresonant background. Solid lines are fit to the data using a sum of two Gaussian peaks. The temperature dependence of the integrated intensity extracted from the fit is shown as black circles and red squares in the inset for the broad background and the sharp peak, respectively. Temperature readings were strongly fluctuating during the measurement depending on the position of the tip of the thermocouple. Values given in the legend and the inset should therefore be taken as a rough estimation of the sample temperature. (a)–(d) were obtained at 4-ID at NSLS-II. However, the rocking curve in (a) was obtained in a different experiment from the rest. \mathbf{Q} scans along (e) H (f), K (g), and L at $\mathbf{Q} = (1, 1, 7)$ in the $\sigma\text{-}\sigma'$ channel and off resonance in the $\sigma\text{-}\pi'$ channel. The intensity is normalized with respect to the peak intensity. The H, K, L values of the peak position are designated to be zero in all plots.

background. On the other hand, only a broad background remains when the nonresonant energy E_{nr} is used. Combining Figs. 1(c) and 2(a), we conclude that the $\sigma\text{-}\pi'$ channel elastic intensity near $\mathbf{Q} = (1, 1, 5)$ consists of two parts: a resonant contribution very sharp in \mathbf{Q} and a nonresonant contribution much broader in \mathbf{Q} .

The existence of a sharp resonant peak on top of a diffuse nonresonant background is also observed at other $\mathbf{Q} = (\text{odd},$

odd, odd), such as $\mathbf{Q} = (1, 1, 3)$ [Fig. 2(b)] and $\mathbf{Q} = (1, 1, 7)$ [Fig. 2(c)]. To understand the origins of the resonant and nonresonant contributions to the diffraction intensity, we show rocking curves at $\mathbf{Q} = (1, 1, 7)$ using the resonant incident energy in Fig. 2(d) at different temperatures. As temperature increases towards T_C , the sharp peak is clearly suppressed, while the diffuse background [shaded region in Fig. 2(d)] is unchanged. Quantitatively, the rocking curve at each temperature is fit to a sum of a sharp Gaussian peak and a broad Gaussian peak. The width of the broad peak is determined independently by fitting to the E_{nr} data at the same \mathbf{Q} . The temperature dependence of the integrated intensity [inset of Fig. 2(d)] clearly shows the intensity of the sharp peak decreases with temperature, while that of the broad background is unchanged. The strong temperature dependence and the clear resonance behavior confirms the sharp peak's magnetic origin. On the other hand, the absence of these characteristics indicates that the nonresonant background is of a structural origin. Since Cr and Re magnetic moments are antiparallel in ferrimagnetically ordered $\text{Sr}_2\text{CrReO}_6$, the magnetic unit cell is the same as the structural unit cell shown in Fig. 1(a). The magnetic Bragg peak therefore coincides with the structural Bragg peak. Although charge scattering is ideally detected only in the $\sigma\text{-}\sigma'$ channel, some of the charge scattering intensity can leak into the $\sigma\text{-}\pi'$ channel as the analyzer is not 100% efficient in removing scattered x rays with σ' polarization. The charge scattering origin of the nonresonant background is further corroborated by Figs. 2(e)–2(g), where we compare \mathbf{Q} scans of the nonresonant background in the $\sigma\text{-}\pi'$ channel to \mathbf{Q} scans in the $\sigma\text{-}\sigma'$ channel, which is sensitive to charge scattering due to structural Bragg peaks. Clearly, their line shapes are identical along all directions, further confirming their common structural origin.

Magnetic scattering intensity in the $\sigma\text{-}\pi'$ channel is proportional to the projection of the ordered moment \mathbf{M} along the direction of the scattered wave vector, or $|\mathbf{M} \cdot \mathbf{k}_f|^2$ [30]. Therefore, information about the direction of \mathbf{M} can be obtained by examining the intensity variation as a function of the azimuthal angle ψ [see Fig. 1(b) for a definition] as the sample is rotated around \mathbf{Q} [27–29,31]. Two issues need to be addressed when extracting magnetic intensity at a given ψ . First, the nonresonant structural background needs to be removed to obtain the resonant magnetic contribution. Second, one needs to account for an overall intensity modulation due to the changing x-ray footprint and hence the probed sample volume as the sample is rotated. This effect is illustrated in the inset of Fig. 3(a): The tail due to the diffuse structural background is larger at smaller sample angles where the x ray is incident on the sample from a more grazing direction. To correct for this effect, each θ scan is normalized with respect to the tail at $\theta \geq 0.05^\circ$ away from the peak position where the resonant magnetic contribution is suppressed. At each azimuthal angle, the nonresonant background was separately measured using a nonresonant incident energy, which is then scaled and subtracted from the normalized θ scans. The resulting θ scans shown in the main panel of Fig. 3(a), corresponding to those of the resonant magnetic signal, are then integrated to extract the magnetic intensity as a function of azimuthal angle.

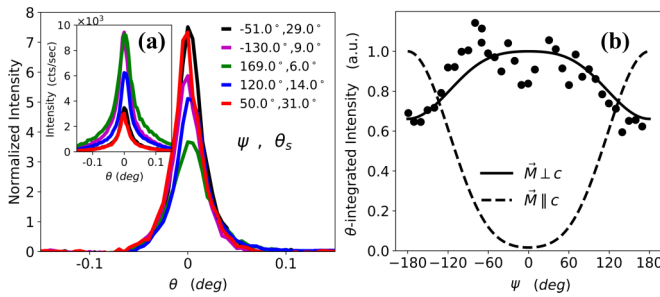


FIG. 3. (a) θ scans of the $\mathbf{Q} = (1, 1, 5)$ magnetic Bragg peak at different azimuthal angles ψ . The legend also shows the corresponding sample angle θ_s , which measures the sample rotation in the scattering plane from perfect grazing geometry. All θ scans are first normalized with respect to the diffuse tail with $\theta \geq 0.05^\circ$ before a separately measured nonresonant background is scaled and subtracted to obtain the magnetic signal. The inset shows the raw θ scans before normalization and background subtraction. (b) Azimuthal dependence of the θ -integrated intensity. The solid (dashed) line is the calculated azimuthal dependence at (1,1,5) for an ordered moment perpendicular (parallel) to the c axis. The reference wave vector is $\mathbf{Q}_{\text{ref}} = (1, 1, 0)$.

The resultant azimuthal dependence of magnetic intensity at $\mathbf{Q} = (1, 1, 5)$ is shown in Fig. 3(b). Another way to obtain the azimuthal dependence from energy scans [e.g., Fig. 1(c)] is shown in the Supplemental Material [23], which gives results identical to those in Fig. 3(b). In a tetragonal crystal such as the $\text{Sr}_2\text{CrReO}_6$ thin film (see the Supplemental Material [23]), the magnetic moments are either parallel or perpendicular to the c axis by symmetry. In Fig. 3(b), simulated azimuthal dependence is shown by the solid (dashed) line for ordered moments perpendicular (parallel) to the c axis. Our data clearly agree with the solid line, suggesting that the ordered moment is perpendicular to the c direction. However, the precise ordering direction within the ab plane could not be determined because of averaging over two orthogonal magnetic domains that are present due to tetragonal crystal symmetry. Our observation of in-plane ordered moments provides a natural explanation for earlier bulk magnetization data [32] which observed a larger magnetic susceptibility in the ab plane than along the c axis (see the Supplemental Material for the M versus H data for our sample [23]).

B. L_3 edge

Although the results in the last section are for the Re L_2 edge, similar results are obtained at the L_3 edge. The energy dependence at ($\theta = \theta_{\text{peak}}$) and slightly off ($\theta = \theta_{\text{peak}} - 0.05^\circ$) the Bragg peak at $\mathbf{Q} = (1, 1, 5)$ is shown in Fig. 4(a). The energy dependence of x-ray fluorescence is also shown for comparison. Clearly, a resonant feature is observed slightly below the absorption maximum at $E_f = 10.536$ keV. When the sample is rotated slightly away from the Bragg peak position, the resonant feature disappears, and the diffraction intensity is minimized at the absorption maximum, typical of the energy dependence of a nonresonant structural Bragg peak [27,28]. We note that the relative intensity of the nonresonant background leaked into the σ - π' channel from the σ - σ' channel is higher at the L_3 edge than at the L_2 edge, possibly due to different analyzers used at the two edges. We

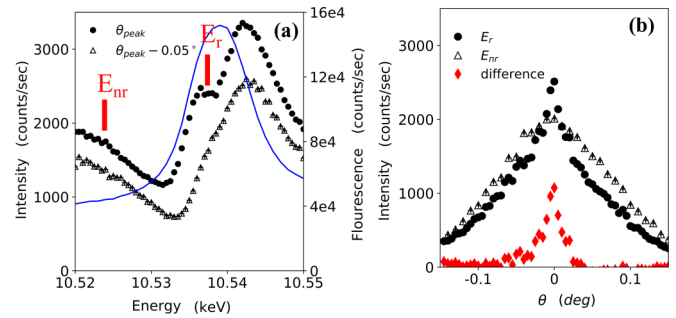


FIG. 4. (a) Energy dependence of the σ - π' channel elastic intensity at $\mathbf{Q} = (1, 1, 5)$ at the Re L_3 edge. The energy dependence is obtained for different θ 's. Data shown by solid black circles are obtained for θ that maximizes the Bragg peak intensity, or θ_{peak} , while those shown by open triangles are obtained 0.05° away from θ_{peak} . The energy dependence of the x-ray fluorescence is shown by the blue solid line. (b) θ scan at $\mathbf{Q} = (1, 1, 5)$ near the L_3 edge, obtained with both the resonant ($E_r = 10.536$ keV) and nonresonant ($E_{\text{nr}} = 10.524$ keV) energies. Data shown by red diamonds give the θ scan of the resonant magnetic signal after scaling and subtracting the nonresonant background.

have checked that θ scans of the resonant and nonresonant contributions at the L_3 edge [Fig. 4(b)] are identical to those at the L_2 edge. Moreover, as we show in the Supplemental Material [23], an azimuthal dependence similar to that shown in Fig. 3(b) is obtained at the L_3 edge after proper normalization and background subtraction. Since the initial states of the REXS processes at the L_2 and L_3 edges are the $2p_{1/2}$ and $2p_{3/2}$ core levels with different selection rules, the relative intensities of the REXS signal at the two edges are expected to reveal information about the electronic ground states in a material. For example, the absence of any magnetic REXS signal at the Ir L_2 edge in $5d$ iridates is consistent with a simple atomic picture where the local ground states are controlled by dominant spin-orbit coupling [26]. Although we cannot directly compare the L_2 and L_3 edges intensities in our experiment due to different analyzers being used at the two edges, a large REXS signal observed at the Re L_2 edge clearly shows that the simple atomic picture applicable to iridates fails in $\text{Sr}_2\text{CrReO}_6$, probably due to the itinerant nature of the Re electrons [33,34]. Notably, observation of a large L_2 REXS signal is also consistent with earlier XMCD measurements [35–37]

IV. DISCUSSION

The most surprising result in our study is the coexistence of a sharp magnetic Bragg peak and a diffuse structural peak at $\mathbf{Q} = (\text{odd}, \text{odd}, \text{odd})$. This important result is emphasized in Fig. 5(a), where we directly compare the rocking curves for the structural and magnetic Bragg peaks at $\mathbf{Q} = (1, 1, 7)$, whose intensities are maximized in the σ - σ' and σ - π' channels, respectively. By fitting the structural Bragg peak at $\mathbf{Q} = (1, 1, 7)$ to a Gaussian, its half width at half maximum [after converting to momentum transfer perpendicular to (1,1,7)] is found to be $\kappa = 0.0065(6) \text{ \AA}^{-1}$. In contrast, the structural Bragg peak at $\mathbf{Q} = (\text{even}, \text{even}, \text{even})$ is resolution limited, as shown in Fig. 5(a). This is entirely consistent with the

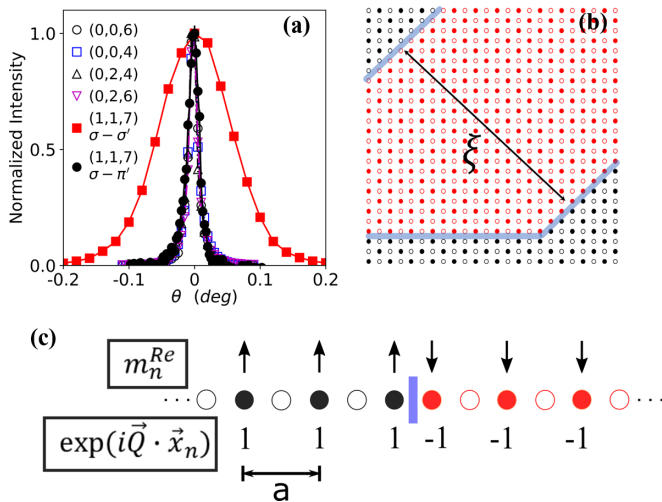


FIG. 5. (a) Comparison between the L_2 edge rocking curves at even \mathbf{Q} 's (open symbols) and $\mathbf{Q} = (1, 1, 7)$ (solid symbols). For $\mathbf{Q} = (1, 1, 7)$, data from both the $\sigma-\pi'$ and $\sigma-\sigma'$ polarization channels are shown. The $\sigma-\pi'$ data at $\mathbf{Q} = (1, 1, 7)$ are the magnetic intensity obtained by subtracting the nonresonant diffuse background. The peak intensities of all rocking curves have been scaled to 1 for comparison. (b) Schematic drawing of APDs separated by APBs (thick lines) in our sample. Open and solid circles denote Cr and Re atoms, respectively. The average domain size is indicated by ξ . Red and black denote the two types of domains where positions of Cr and Re ions are exchanged. (c) One-dimensional model of the APB (thick vertical line in the middle). The two domains are colored black and red as in (b). Re magnetic moments m_n^{Re} are shown by black vertical arrows above each Re atoms. The phase factor $\exp(i\vec{Q} \cdot \vec{x}_n)$ used to calculate the magnetic Bragg peak intensity at odd \mathbf{Q} 's is shown below each Re atom.

presence of AS disorder in the sample. To see this, we note that contribution to the scattering amplitude at even and odd \mathbf{Q} 's by a nearest-neighbor pair of ions, Re and Cr, is proportional to $f_{Re} + f_{Cr}$ and $f_{Re} - f_{Cr}$, respectively, with f_{Re} and f_{Cr} being the atomic form factors. Therefore, only odd \mathbf{Q} 's will be sensitive to the existence of APD in the sample where locations of Re and Cr are exchanged for neighboring domains [see Fig. 5(b) for a schematic drawing of an AS disordered DP crystal with APDs]. This leads to selective broadening of structural Bragg peaks at odd \mathbf{Q} 's that has been observed in other DPs with APDs [17,38]. The correlation length extracted from the inverse of broadening in \mathbf{Q} scans therefore gives the average APD size ξ . Using $\kappa = 0.0065(5) \text{ \AA}^{-1}$, this is estimated to be $\xi = \frac{1}{\kappa} = 15(2) \text{ nm}$ in our $\text{Sr}_2\text{CrReO}_6$ sample. By comparing the 319-nm film used here to a 90-nm film (see the Supplemental Material [23]), we confirmed the existence of larger APDs in a sample with a lower level of AS disorder.

Having established the presence of APD in $\text{Sr}_2\text{CrReO}_6$, we now move on to discuss its effect on the magnetic order. Naively, one expects proliferation of random structural defects such as the APBs to adversely affect the magnetic order and limit magnetic correlation to *within* individual APDs. However, this is directly contradicted by our data showing a much sharper magnetic Bragg peak at the *same* \mathbf{Q} 's where the structural Bragg peak is broadened by the finite size of APDs.

Remarkably, as shown in Fig. 5(a), the magnetic Bragg peaks have almost the same width as the sharp resolution-limited structural Bragg peaks at even \mathbf{Q} 's. We therefore arrive at the important conclusion that the magnetic correlation extends far beyond the APBs in $\text{Sr}_2\text{CrReO}_6$. Quantitatively, a lower bound for magnetic correlation length is estimated to be $\sim 90 \text{ nm}$ from the width of the magnetic Bragg peak.

Microscopically, this implies that two neighboring APDs must be strongly magnetically coupled in $\text{Sr}_2\text{CrReO}_6$. Since the APB separating the two neighboring domains consists of 180° Re-O-Re or Cr-O-Cr bonds, simple application of Goodenough-Kanomori rules suggests that two neighboring domains are antiferromagnetically coupled. Schematically, we illustrate the resulting magnetic and structural arrangement of two neighboring domains using a heuristic one-dimensional (1D) chain model in Fig. 5(c), where solid and open circles denote Re and Cr atoms, respectively (the same argument holds true in three dimensions). Within each domain, the Re and Cr moments are antiferromagnetically coupled, leading to a ferromagnetic arrangement of Re moments shown by black vertical arrows (the Cr moment is not shown). Across the APB (denoted by the vertical line), all Re moments are flipped with respect to the first domain. The magnetic Bragg peak intensity at a given \mathbf{Q} is proportional to the square of $\sum_n m_n^{Re} \exp(i\vec{Q} \cdot \vec{x}_n)$, where \sum_n is the sum over all Re sites and m_n^{Re} is the Re magnetic moment at site n . In the 1D model, phase factors $\exp(i\vec{Q} \cdot \vec{x}_n)$ for odd \mathbf{Q} 's [equivalent to $\mathbf{Q} = (\text{odd}, \text{odd}, \text{odd})$ in a three-dimensional model] are shown for the two neighboring domains in Fig. 5(c). Very importantly, as the phase factor changes sign at the APB, the magnetic moment m_n^{Re} changes sign as well. Magnetic scattering amplitudes for two antiferromagnetically coupled APDs therefore add constructively at odd \mathbf{Q} 's. This provides a microscopic explanation for why magnetic Bragg peaks at odd \mathbf{Q} 's remain sharp in our data, while the structural Bragg peaks are broadened.

V. CONCLUSIONS

In conclusion, we have carried out REXS at the Re L_2 and L_3 edges to study room temperature structural and magnetic correlation in a thin-film sample of a high- T_C DP, $\text{Sr}_2\text{CrReO}_6$. We showed directly that the ordered moments lie perpendicular to the c axis, which explained the earlier bulk magnetization data. More importantly, we found very different structural and magnetic correlation lengths in the sample; the former is limited by the sizes of the antiphase domains of about 15 nm, while the latter is at least 90 nm, far exceeding the average domain size. Our results are consistent with antiferromagnetically coupled APDs. The existence of magnetically correlated APDs has been argued to enhance the magnetoresistance of a DP sample, and hence its performance as a spintronic material, due to cooperative spin rotation between different domains [21]. Our work can be readily extended to systematically study the magnetic and structural correlations in thin-film samples with different levels of AS disorder [39]. Furthermore, excellent momentum resolution combined with large penetration depth of x rays also enables one to study the relationship between APDs and magnetic correlations in other DP single crystals.

ACKNOWLEDGMENTS

Work at the University of Toronto was supported by the Natural Science and Engineering Research Council (NSERC) of Canada, Canada Foundation for Innovation (CFI), and Ontario Research Fund (ORF) – Large Infrastructure. Work at The Ohio State University was supported by the Center for

Emergent Materials, a National Science Foundation–funded Materials Research Science and Engineering Centers, under Grant No. DMR-2011876. This research used beamline 4-ID of the National Synchrotron Light Source II, a U.S. Department of Energy (DOE) Office of Science User Facility operated for the DOE Office of Science by Brookhaven National Laboratory under Contract No. DE-SC0012704.

-
- [1] D. Serrate, J. M. D. Teresa, and M. R. Ibarra, *J. Phys.: Condens. Matter* **19**, 023201 (2006).
- [2] Y. Tomioka, T. Okuda, Y. Okimoto, R. Kumai, K.-I. Kobayashi, and Y. Tokura, *Phys. Rev. B* **61**, 422 (2000).
- [3] K.-I. Kobayashi, T. Kimura, H. Sawada, K. Terakura, and Y. Tokura, *Nature (London)* **395**, 677 (1998).
- [4] H. Kato, T. Okuda, Y. Okimoto, Y. Tomioka, Y. Takenoya, A. Ohkubo, M. Kawasaki, and Y. Tokura, *Appl. Phys. Lett.* **81**, 328 (2002).
- [5] A. J. Hauser, J. R. Soliz, M. Dixit, R. E. A. Williams, M. A. Susner, B. Peters, L. M. Mier, T. L. Gustafson, M. D. Sumption, H. L. Fraser, P. M. Woodward, and F. Y. Yang, *Phys. Rev. B* **85**, 161201(R) (2012).
- [6] H. Asano, N. Kozuka, A. Tsuzuki, and M. Matsui, *Appl. Phys. Lett.* **85**, 263 (2004).
- [7] J. M. De Teresa, D. Serrate, C. Ritter, J. Blasco, M. R. Ibarra, L. Morellon, and W. Tokarz, *Phys. Rev. B* **71**, 092408 (2005).
- [8] S. Geprägs, F. Czeschka, M. Opel, S. Goennenwein, W. Yu, W. Mader, and R. Gross, *J. Magn. Magn. Mater.* **321**, 2001 (2009).
- [9] Y. Krockenberger, K. Mogare, M. Reehuis, M. Tovar, M. Jansen, G. Vaitheeswaran, V. Kanchana, F. Bultmark, A. Delin, F. Wilhelm, A. Rogalev, A. Winkler, and L. Alff, *Phys. Rev. B* **75**, 020404(R) (2007).
- [10] K. Samanta, P. Sanyal, and T. Saha-Dasgupta, *Sci. Rep.* **5**, 15010 (2015).
- [11] O. El Rhazouani, Z. Zarhri, A. Benyoussef, and A. El Kenz, *Phys. Lett. A* **380**, 1241 (2016).
- [12] J. M. Greneche, M. Venkatesan, R. Suryanarayanan, and J. M. D. Coey, *Phys. Rev. B* **63**, 174403 (2001).
- [13] J. Navarro, L. Balcells, F. Sandiumenge, M. Bibes, A. Roig, B. Martínez, and J. Fontcuberta, *J. Phys.: Condens. Matter* **13**, 8481 (2001).
- [14] X. Yu, T. Asaka, Y. Tomioka, C. Tsuruta, T. Nagai, K. Kimoto, Y. Kaneko, Y. Tokura, and Y. Matsui, *J. Electron Microsc.* **54**, 61 (2005).
- [15] T. Asaka, X. Z. Yu, Y. Tomioka, Y. Kaneko, T. Nagai, K. Kimoto, K. Ishizuka, Y. Tokura, and Y. Matsui, *Phys. Rev. B* **75**, 184440 (2007).
- [16] B. D. Esser, A. J. Hauser, R. E. A. Williams, L. J. Allen, P. M. Woodward, F. Y. Yang, and D. W. McComb, *Phys. Rev. Lett.* **117**, 176101 (2016).
- [17] C. Meneghini, S. Ray, F. Liscio, F. Bardelli, S. Mobilio, and D. D. Sarma, *Phys. Rev. Lett.* **103**, 046403 (2009).
- [18] J. Navarro, J. Nogués, J. S. Muñoz, and J. Fontcuberta, *Phys. Rev. B* **67**, 174416 (2003).
- [19] D. Sánchez, J. A. Alonso, M. García-Hernández, M. J. Martínez-Lope, J. L. Martínez, and A. Mellergård, *Phys. Rev. B* **65**, 104426 (2002).
- [20] S. Pal, S. Govinda, M. Goyal, S. Mukherjee, B. Pal, R. Saha, A. Sundaresan, S. Jana, O. Karis, J. W. Freeland, and D. D. Sarma, *Phys. Rev. B* **97**, 165137 (2018).
- [21] V. N. Singh and P. Majumdar, *Europhys. Lett.* **94**, 47004 (2011).
- [22] G. van der Laan, *C. R. Phys.* **9**, 570 (2008).
- [23] See Supplemental Material at <http://link.aps.org/supplemental/10.1103/PhysRevB.103.064410> for sample characterization information and additional REXS data.
- [24] D. F. McMorrow, S. E. Nagler, K. A. McEwen, and S. D. Brown, *J. Phys.: Condens. Matter* **15**, L59 (2003).
- [25] D. Hirai, H. Sagayama, S. Gao, H. Ohsumi, G. Chen, T.-h. Arima, and Z. Hiroi, *Phys. Rev. Research* **2**, 022063(R) (2020).
- [26] B. J. Kim, H. Ohsumi, T. Komesu, S. Sakai, T. Morita, H. Takagi, and T. Arima, *Science* **323**, 1329 (2009).
- [27] X. Liu, T. Berlijn, W.-G. Yin, W. Ku, A. Tsvelik, Y.-J. Kim, H. Gretarsson, Y. Singh, P. Gegenwart, and J. P. Hill, *Phys. Rev. B* **83**, 220403(R) (2011).
- [28] A. Biffin, R. D. Johnson, I. Kimchi, R. Morris, A. Bombardi, J. G. Analytis, A. Vishwanath, and R. Coldea, *Phys. Rev. Lett.* **113**, 197201 (2014).
- [29] S. Boseggia, R. Springell, H. C. Walker, H. M. Rønnow, C. Rüegg, H. Okabe, M. Isobe, R. S. Perry, S. P. Collins, and D. F. McMorrow, *Phys. Rev. Lett.* **110**, 117207 (2013).
- [30] J. P. Hill and D. F. McMorrow, *Acta Crystallogr., Sect. A* **52**, 236 (1996).
- [31] S. H. Chun, J.-W. Kim, J. Kim, H. Zheng, C. C. Stoumpos, C. D. Malliakas, J. F. Mitchell, K. Mehlawat, Y. Singh, Y. Choi, T. Gog, A. Al-Zein, M. M. Sala, M. Krisch, J. Chaloupka, G. Jackeli, G. Khaliullin, and B. J. Kim, *Nat. Phys.* **11**, 462 (2015).
- [32] J. M. Lucy, M. R. Ball, O. D. Restrepo, A. J. Hauser, J. R. Soliz, J. W. Freeland, P. M. Woodward, W. Windl, and F. Y. Yang, *Phys. Rev. B* **90**, 180401(R) (2014).
- [33] B. Yuan, J. P. Clancy, A. M. Cook, C. M. Thompson, J. Greedan, G. Cao, B. C. Jeon, T. W. Noh, M. H. Upton, D. Casa, T. Gog, A. Paramekanti, and Y.-J. Kim, *Phys. Rev. B* **95**, 235114 (2017).
- [34] B. Yuan, J. P. Clancy, J. A. Sears, A. I. Kolesnikov, M. B. Stone, Z. Yamani, C. Won, N. Hur, B. C. Jeon, T. W. Noh, A. Paramekanti, and Y.-J. Kim, *Phys. Rev. B* **98**, 214433 (2018).
- [35] A. J. Hauser, J. M. Lucy, M. W. Gaultois, M. R. Ball, J. R. Soliz, Y. Choi, O. D. Restrepo, W. Windl, J. W. Freeland, D. Haskel, P. M. Woodward, and F. Yang, *Phys. Rev. B* **89**, 180402(R) (2014).

- [36] V. N. Antonov, S. Uba, L. Uba, L. V. Bekenov, and A. Bonda, *Phys. Rev. B* **98**, 064414 (2018).
- [37] P. Majewski, S. Geprägs, O. Sanganas, M. Opel, R. Gross, F. Wilhelm, A. Rogalev, and L. Alff, *Appl. Phys. Lett.* **87**, 202503 (2005).
- [38] S. Chakraverty, A. Ohtomo, D. Okuyama, M. Saito, M. Okude, R. Kumai, T. Arima, Y. Tokura, S. Tsukimoto, Y. Ikuhara, and M. Kawasaki, *Phys. Rev. B* **84**, 064436 (2011).
- [39] S. Chakraverty, A. Ohtomo, and M. Kawasaki, *Appl. Phys. Lett.* **97**, 243107 (2010).